Photoexcitation Dynamics in Nanomaterials

Oleg V. Prezhdo*, Walter R. Duncan, Colleen F. Craig, Svetlana V. Kilina, and Brad F. Habenicht

Department of Chemistry, University of Washington, Seattle, WA 98195-1700, USA

Abstract

Non-adiabatic molecular dynamics (NAMD) implemented within the time-dependent density functional formalism (TDDFT) is applied to study ultrafast photoinduced dynamics in novel nanoscale materials, including dye and polymer sensitized semiconductors, quantum dots and carbon nanotubes. The classical-path, mean-field and surface-hopping approaches to NAMD are formulated within TDDFT for electron-nuclear dynamics. Particular attention will be given to

a) The interfacial electron injection from molecular and polymeric chromophores into the TiO2 surface, which drives the Gratzel solar cell and illustrates the molecule-semiconductor contact problem in molecular electronics and photoelectrochemistry.

b) The electron-vibrational and Auger relaxations of photoexcited states in quantum dots (QD), which determine the efficiencies of hot carrier accumulation and carrier multiplication in QD solar cells.

c) The electron-phonon scattering in carbon nanotubes, which affects conductivity and characterizes nanotube potential for use in nanoscale electronic devices.

1 Introduction

Rapid advances in chemical synthesis and fabrication techniques generate novel types of materials that exhibit original and often unforeseen properties and phenomena. These are immediately studied by physical detection tools that probe material response to a variety of perturbations. The experimental data generated in such measurements demand understanding and interpretation that are greatly facilitated by theoretical modeling and simulation. The current chapter presents three closely related theoretical studies of charge transfer and relaxation phenomena recently observed in novel nanoscale materials using ultrafast laser spectroscopies. The materials under investigation are the molecule-semiconductor interface and the two types of quantum confinement devices, including the quasi-zero-dimensional quantum dots (QD) and quasi-one-dimensional carbon nanotubes (CN). The motivation for the studies largely stems from the search for alternative energy sources. The materials under investigation have the potential to replace the existing solar cells with more efficient designs and to generate chemically stored energy, such as hydrogen obtained by splitting water. The questions raised by the experimental observations and elucidated by the described simulations bear on a wide range of problems encountered in molecular and nanoscale electronics, spintronics and quantum information processing, biological imaging and detection, etc.

The first problem addressed below deals with the photoinduced charge transfer across a molecule-semiconductor interface. The system originates from the Grätzel type solar cell and provides an excellent example of numerous issues that arise when two fundamentally different types of systems are brought together. Molecules, typically studied by chemists, show finite sets of discrete, localized quantum states. Bulk semiconductors, on the other hand, are studied by physicists, and are characterized by continuous bands of delocalized orbitals. The intrinsic difference in the quantum states of the two systems, as well as the

* Corresponding Author, E-mail: prezhdo@u.washington.edu

often disparate sets of theories and experimental tools used by chemists and physicists, create challenges for the study of the molecule-semiconductor interface. Similar issues arise in nanoscale electronics, where small molecular objects are sandwiched between bulk electrodes.

The second and third projects tackle charge and energy relaxation in recently created materials showing quantum confinement effects. Originally considered to be nanoscale derivatives of bulk materials with related properties, QDs and CNs have taken on a life of their own and are now often regarded as artificial atoms and nanowires, due to their close resemblance to traditional molecular objects. Yet QDs and CNs are in neither the bulk nor molecular regime, and each exhibit an entirely new range of properties placing them squarely in between the two traditional types of materials. The study of the electron and hole relaxation in the QDs reported below is prompted by the recent experimental detection of multiple charge carriers generated upon absorption of only a single photon. The study investigates the mechanisms for increasing the current and voltage in photovoltaic cells and also directly relates to spintronic and quantum computing applications of quantum dots, in particular by establishing the limits on vibrationally induced dephasing that must be avoided. The electron and hole relaxation facilitated by phonons results in CN heating and is critical to understand for successful development of nanotube-based miniature electronic devices. The relaxation plays a key role in CN- and fullerene-based photovoltaic designs.

The simulations described below became possible with the development of the state-of-the-art theoretical tools designed to tackle the specific problems, which resulted in theoretical advances important in their own regard. The theoretical approaches are explained in the next section, which is followed by the sections on the molecule-semiconductor charge injection, the excitation dynamics in QDs and the electron and hole relaxation in CNs. The chapter concludes with a summary and a broader prospective of the key results.

2 Theoretical Approaches

The simulations are performed using the time-dependent (TD) Kohn-Sham (KS) density functional theory (DFT) for electron-nuclear dynamics, where the electrons are described quantum-mechanically, while the much heavier and slower nuclei are treated classically. Three variants of the theory are used. They share the same equations for the electronic evolution and differ in the implementation of the nuclear dynamics that is chosen depending on the problem under consideration and computational simplicity. DFT provides a modern and versatile means for the investigation of molecular and solid state structures, reaction pathways, thermochemistry, dipole moments, spectroscopic response, and many other properties.[1,2] It is accurate, flexible, and computationally efficient compared to the Hartree-Fock and post-Hartree-Fock methods.[3] The electron-nuclear TDKS theory is implemented within the VASP code that provides a commercially available distribution of time-independent DFT.[4,5]

Time-Dependent Kohn-Sham Theory for Electron-Nuclear Dynamics

The electron density is the central quantity in DFT. It is represented in the KS theory[6] as the sum over single-electron KS orbitals $\varphi_p(x,t)$

$$\rho(x,t) = \sum_{p=1}^{N_e} |\varphi_p(x,t)|^2 , \tag{1}$$

where N_e is the number of electrons. The time-evolution of $\varphi_p(x,t)$ is determined by application of the Dirac TD variational principle to the KS energy

$$E\{\varphi_p\} = \sum_{p=1}^{N_e} \langle \varphi_p | K | \varphi_p \rangle + \sum_{p=1}^{N_e} \langle \varphi_p | V | \varphi_p \rangle + \frac{e^2}{2} \int\int \frac{\rho(x',t)\rho(x,t)}{|x-x'|} d^3x d^3x' + E_{xc}. \tag{2}$$

The right-hand side of Eq. 2 gives the kinetic energy of noninteracting electrons, the electron-nuclear attraction, the Coulomb repulsion of density $\rho(x,t)$, and the exchange-correlation energy functional that accounts for the residual many-body interactions. Application of the variational principle leads to a system of single-particle equations[1,2,7–9]

$$i\hbar\frac{\partial\varphi_p(x,t)}{\partial t} = H(\varphi(x,t))\varphi_p(x,t),\ p=1,\ldots,N_e, \tag{3}$$

where the Hamiltonian H depends on the KS orbitals. In the generalized gradient approximation[10] used in the current simulations, E_{xc} depends on both density and its gradient, and the Hamiltonian is written as

$$H = -\frac{\hbar^2}{2m_e}\nabla^2 + V_N(x;\mathbf{R}) + e^2\int\frac{\rho(x')}{|x-x'|}d^3x' + V_{xc}\left\{\rho,\nabla\rho\right\}. \tag{4}$$

The KS energy (2) may be expressed as the expectation value of the Hamiltonian with respect to the Slater determinant (SD) formed with the KS orbitals[6]

$$E = \big\langle\varphi_a\,\varphi_b\,\cdots\,\varphi_p\big|H\big|\varphi_a\,\varphi_b\,\cdots\,\varphi_p\big\rangle. \tag{5}$$

The single-electron density (1) is obtained from the SD by tracing over N_e-1 electrons.

$$\rho(x_1) = N_e\ \mathrm{Tr}_{x_2,\ldots,x_{N_e}}|\varphi_a(x_1)\,\varphi_b(x_2)\,\cdots\,\varphi_p(x_{N_e})\rangle\langle\varphi_a(x_1)\,\varphi_b(x_2)\,\cdots\,\varphi_p(x_{N_e})|. \tag{6}$$

The TD KS orbitals $\varphi_p(x,t)$ are expanded in the basis of adiabatic KS orbitals $\widetilde{\varphi}_k\ (x;\mathbf{R})$ that are the single-electron eigenstates of the KS Hamiltonian (4)

$$\varphi_p(x,t) = \sum_k^{N_e} c_{pk}(t)\big|\widetilde{\varphi}_k\ (x;\mathbf{R})\big\rangle. \tag{7}$$

The adiabatic KS orbital basis is readily available from a time-independent DFT calculation[4,5] and provides a preferable representation for one of the nuclear dynamics approaches described below. The TDKS equation (3) transforms in the adiabatic KS basis to the equation for the expansion coefficients

$$i\hbar\frac{\partial}{\partial t}c_{pk}(t) = \sum_m^{N_e} c_{pm}(t)\Big(\epsilon_m\delta_{km} + \mathbf{d}_{km}\cdot\dot{\mathbf{R}}\Big). \tag{8}$$

The non-adiabatic (NA) coupling

$$\mathbf{d}_{km}\cdot\dot{\mathbf{R}} = -i\hbar\big\langle\widetilde{\varphi}_k\ (x;R)\big|\nabla_{\mathbf{R}}\big|\ \widetilde{\varphi}_m\ (x;R)\big\rangle\cdot\dot{\mathbf{R}} = -i\hbar\big\langle\widetilde{\varphi}_k\ \big|\frac{\partial}{\partial t}\big|\ \widetilde{\varphi}_m\big\rangle \tag{9}$$

arises from the dependence of the adiabatic KS orbitals on the nuclear trajectory, and is computed from the right-hand-side of Eq. (9).[11] Similarly to Eq. 7, the time-evolving SD (see Eq. 5) evolves into a superposition of adiabatic SDs

$$\big|\varphi_a\,\varphi_b\,\cdots\,\varphi_p\big\rangle = \sum_{j\neq k\neq\cdots\neq l}^{N_e}\mathcal{C}_{j\,\ldots\,l}(t)\ \Big|\ \widetilde{\varphi}_j\,\widetilde{\varphi}_k\ \cdots\ \widetilde{\varphi}_l\ \Big\rangle \tag{10}$$

with the many-electron coefficients $\mathcal{C}_{j\,\ldots\,l}(t)$ expressed in terms of the single-electron coefficients

$$\mathcal{C}_{j\,\ldots\,l}(t) = c_{pj}(t)\,c_{qk}(t)\,\cdots\,c_{vl}(t). \tag{11}$$

The evolution of $\mathcal{C}_{j\,\ldots\,l}$ follows from Eq. (8)

$$i\hbar\frac{\partial}{\partial t}\mathcal{C}_{q\cdots v}(t) = \sum_{a\cdots p}^{N_e}\mathcal{C}_{a\cdots p}(t)\Big[E_{q\cdots v}\delta_{aq}\cdots\delta_{pv} + \mathbf{D}_{a\cdots p;q\cdots r}\cdot\dot{\mathbf{R}}\Big]. \tag{12}$$

$E_{q\cdots v} = \big\langle\widetilde{\varphi}_q\cdots\widetilde{\varphi}_v\big|H\big|\widetilde{\varphi}_q\cdots\widetilde{\varphi}_v\big\rangle$ is the many-electron eigenenergy, and the many-electron NA coupling

$$\mathbf{D}_{a\cdots p;q\cdots r}\cdot\dot{\mathbf{R}} = -i\hbar\big\langle\widetilde{\varphi}_a\,\widetilde{\varphi}_b\ \cdots\ \widetilde{\varphi}_p\,\big|\frac{\partial}{\partial t}\big|\widetilde{\varphi}_q\,\widetilde{\varphi}_r\ \cdots\ \widetilde{\varphi}_v\,\big\rangle. \tag{13}$$

is non-zero only if the determinants differ in a single KS orbital.

The Classical Path Approximation

The equations above define dynamics of the electronic subsystem evolving in response to the nuclear degrees of freedom that determine the electron-nuclear potential V in the Hamiltonian (4). The nuclear trajectory $\mathbf{R}(t)$ has yet to be defined. While it is common and straightforward to define the effect of the classical nuclei on the quantum electrons through the $\mathbf{R}$-dependence of the electron-nuclear potential, the back-reaction of the electrons on the classical nuclei is not straightforward. Numerous prescriptions have been proposed, each with its own merits.[11–45] All quantum-classical approximations, however, violate some essential properties seen in a fully quantum electron-nuclear dynamics. The classical path approximation (CPA) provides the simplest solution by ignoring the back-reaction and assuming that the classical path is predetermined.[13,14] The CPA is the simplest and computationally most efficient approximation, and is a valid approach if the nuclear dynamics is not sensitive to changes in the electronic subsystem. The classical nuclear trajectory associated with the electronic ground state is often used in cases where excited state potential energy surfaces (PES) are similar to the ground state PES, and where the nuclear kinetic energy and thermal fluctuations of the nuclei are large compared to the differences in the PES.

The Ehrenfest Nuclear Dynamics

The mean-field or Ehrenfest[46] approximation is the simplest form of the back-reaction of electrons on the nuclei. Here, the classical variables couple to the expectation value of the quantum force operator[12–14]

$$M\ddot{\mathbf{R}} = -\big\langle \varphi_a\, \varphi_b\, \cdots\, \varphi_p \big| \nabla_{\mathbf{R}} H \big| \varphi_a\, \varphi_b\, \cdots\, \varphi_p \big\rangle. \tag{14}$$

The gradient $\nabla_{\mathbf{R}}$ is applied directly to the Hamiltonian according to the TD Hellmann-Feynman theorem.[14] Thoroughly investigated by many authors, the Ehrenfest method remains valid under the conditions similar to those needed for the CPA and requires modification when electron-nuclear correlations[16] and detailed balance must be taken into account.[17,47,48] Advanced versions of the Ehrenfest approach include "quantum fluctuation variables", alleviating some problems.[47–57] More radical solutions are provided by other techniques; one of the most popular and efficient is the trajectory surface hopping (SH) approach.[11,14–31]

Surface Hopping

In SH, the nuclear trajectory responds to the electronic forces by stochastically "hopping" between electronic states.[11,14–31] Analytical and numerical arguments have indicated that SH should be performed in the adiabatic representation (7). Among many flavors of SH, the fewest-switches (FS) SH is designed to minimize the number of hops and satisfy a number of other key physical criteria.[16] The nuclear trajectory in SH propagates adiabatically

$$M\ddot{\mathbf{R}} = -\big\langle \widetilde{\varphi}_a\, \widetilde{\varphi}_b\, \cdots\, \widetilde{\varphi}_p \big| \nabla_{\mathbf{R}} H \big| \widetilde{\varphi}_a\, \widetilde{\varphi}_b\, \cdots\, \widetilde{\varphi}_p \big\rangle. \tag{15}$$

rather than in the mean-field, Eq. (14). The probability that the nuclear trajectory hops to another adiabatic state over time interval dt is

$$d\mathrm{P}_{a\cdots p;q\cdots r} = \frac{B_{a\cdots p;q\cdots r}}{A_{a\cdots p;q\cdots r}} dt, \tag{16}$$

where

$$B_{a\cdots p;q\cdots r} = -2\,\mathrm{Re}\big(A^*_{a\cdots p;q\cdots r} \mathbf{D}_{a\cdots p;q\cdots r} \cdot \dot{\mathbf{R}}\big); \quad A_{a\cdots p;q\cdots r} = \mathcal{C}_{a\cdots p}\, \mathcal{C}^*_{q\cdots r}. \tag{17}$$

If the calculated $d\mathrm{P}_{a\cdots p;q\cdots r}$ is negative, the hopping probability is set to zero. After the hop, the nuclear trajectory continues adiabatically in the new state $q\cdots r$. In order to conserve the total electron-nuclear energy after a hop, the nuclear velocities are rescaled[11,16] along the direction of the electronic component of the NA coupling $\mathbf{D}_{a\cdots p;q\cdots r}$. If a NA transition to a higher energy electronic state is predicted by Eq. 16, and the kinetic energy available in the nuclear coordinates along the direction of the NA coupling is insufficient to accommodate the increase in the electronic energy, the hop is rejected. The velocity rescaling and hop rejection produce detailed balance between upward and downward transitions.[17]

The CPA can be adapted to SH in order to achieve computational speed-up and improved statistical sampling. The SH probabilities can be computed based on the ground state nuclear trajectory if the following assumptions hold: 1) that the electronic PES are similar, 2) that the electronic energy dumped after a hop rapidly distributes among all vibrational modes, The detailed balance that is achieved in the original FSSH

by the nuclear velocity rescaling performed after each transition is restored by multiplying the probability of transitions upward in energy by the Boltzmann factor.

While several SH procedures have been derived using the partial Wigner transform techniques,[23–25] most SH approaches remain *ad hoc*. SH can be viewed as a quantum master equation with the transitions probabilities that are computed non-perturbatively and on-the-fly for the current nuclear configuration. In contrast to the traditional quantum master equations, SH is capable of describing the short-time Gaussian component of quantum dynamics that is responsible for the quantum Zeno effect and related phenomena.[30,58–61]

3 Ultrafast Photoinduced Electron Injection in Dye-Sensitized TiO_2

Electron transfer (ET) at organic/inorganic interfaces plays a key role in many areas of research, including molecular electronics,[62–66] photo-electrolysis,[67] photo-catalysis[68–71] and color photography.[72] ET at semiconductor interfaces constitutes the primary step in novel photovoltaic devices comprised of dye-sensitized semiconductors,[73–82] assemblies of inorganic semiconductors with conjugated polymers,[83–86] and quantum confinement devices.[87,88] The exact mechanistic details of the interfacial ET in these materials are an issue of practical importance and theoretical debate.

The alizarin-TiO_2 interface is a particular example of the photoinduced charge separation component in the Grätzel cell, where highly porous nano-crystalline titanium dioxide is sensitized with transition metal or organic dye molecules.[73–75] Grätzel cells offer a promising alternative to the more costly traditional solar cells. Absorption of light excites the dye-sensitizer molecules from their ground state, which is located energetically in the semiconductor band gap, to an excited state that is resonant with the TiO_2 conduction band (CB) (Fig. 1). The electron is then transferred on the ultrafast timescale to the semiconductor, which is in contact with one of the electrodes. Upon carrying an electric load and reaching the second electrode, the electron enters an electrolyte that carries it back to the chromophore ground state. Ultrafast laser techniques have shown that electron injection can occur in less than 100 fs,[76–82] making it difficult to invoke traditional ET models, which require slow ET dynamics to allow for redistribution of vibrational energy.[77]

Direct modeling of the ultrafast electron injection processes between dyes and semiconductors observed in laser experiments has been performed with reduced models and a full quantum-mechanical description of electrons and nuclei[81,89,90] and at a detailed atomistic level using a quantum description of electrons and classical treatment of nuclei.[91–98] The first real-time *ab initio* atomistic simulations of the interfacial ET from isonicotinic acid into TiO_2 were carried out in our group.[92–94] The dye was chosen to have an excited state well within the semiconductor CB, since the researchers usually assume that a high density of semiconductor states is needed for fast and efficient ET.[73–76,99–101]

The alizarin/TiO_2 system investigated in our group most recently represents an interesting and novel case in which the photoexcited state is positioned near the band edge. The experiments show that electron injection from the alizarin excited state near the TiO_2 CB edge is no less efficient than ET from chromophores with excited states deep in the CB. Moreover, the injection is extremely fast with a record 6 fs transfer time.[80] Efficient ultrafast injection from photoexcited states near the CB edge is both fundamentally interesting and practically important. The fundamental question is: what mechanisms make the ET so fast in the absence of a high density of acceptor states? On the practical side, injection at the CB edge has the potential to aid in the design of cells with higher maximum theoretical voltage, since energy will not be lost by rapid relaxation to the bottom of the CB.[102] We have modeled the injection dynamics by the classical path approximation in the *ab initio* TDKS theory described in the previous section. The simulation has uncovered a number of novel features of the injection process that are not observed in the previously studied cases.[73–82,89–94]

Nuclear Dynamics

Nuclear dynamics have a two-fold influence on the ultrafast electron injection process. On the one hand, thermal fluctuations of the nuclei create an ensemble of initial conditions with slightly different geometries and photoexcitation energies. On the other hand, upon photoexcitation, nuclei drive ET by moving along the reaction coordinate and, alternatively, by inducing direct quantum transitions between the donor and acceptor states. The evolution of the photoexcited and CB state energies is presented in Fig. 2. The fluctuation of the energies at room temperature is sufficient to move the photoexcited state into and out of the TiO_2 conduction band, generating two ET regimes. Outside of the band the coupling of the chromophore excited

state to the semiconductor states is small. Inside the band the density of states (DOS) grows substantially with increasing energy, and the chromophore excited state can therefore interact with a larger number of TiO_2 states. The Fourier transform (FT) of the photoexcited state energy is shown in the insert of Figs. 2. The main contributions to the energy fluctuation are seen at the frequencies below 700 cm^{-1}, corresponding to bending and torsional motions. Small peaks are seen up to 1600 cm^{-1}, characteristic of the C-C and C=O stretches. Vibrations above 1600 cm^{-1} do not contribute to the oscillation of the photoexcited state energy, although the do contribute to the fluctuation of the photoexcited state localization.[96]

Distribution of Initial Conditions for ET

Thermal fluctuations of atomic coordinates produce a distribution of the photoexcited state energies and localizations that creates an inhomogeneous ensemble of initial conditions for the electron injection. Below the CB edge the TiO_2 DOS is low, and there is very little mixing between the alizarin excited state and the semiconductor, Fig. 3. The localization of the photoexcited state on the alizarin molecule (filled circles) is therefore close to one. As the energy increases, progressively more CB states couple to the chromophore. Under these circumstances the localization decreases (empty circles) and significant amounts of ET occur already during the photoexcitation. The large spread in the localization data at higher energies is due to fluctuations in the surface that cause changes in the energies and spatial extent and localization of the semiconductor surface states. The number of semiconductor states that the chromophore can couple to at a particular energy varies with the atomic configuration. Even if the density of acceptor states is the same, the spatial overlap between these states and the chromophore excited state vary substantially, depending on the current geometry of the docking region. Despite the spread of the localization data, there is a clear difference between the photoexcited states below and above the CB edge.

The Mechanism of Electron Injection

Two competing ET mechanisms have been proposed to explain the observed ultrafast injection events.[76] These mechanisms have drastically different implications for the variation of the interface conductance and solar cell voltage with system properties. In the adiabatic mechanism, the coupling between the dye and the semiconductor is large, and the ET occurs through a transition state (TS) along the reaction coordinate that involves a concerted motion of nuclei. During adiabatic transfer, the electron remains in the same Born-Oppenheimer (adiabatic) state that continuously changes its localization from the dye to the semiconductor along the reaction coordinate. A small TS barrier relative to the nuclear kinetic energy gives fast adiabatic ET. NA effects decrease the amount of ET that happens at the TS, but open up a new channel involving direct transitions from the dye into the semiconductor that can occur at any nuclear configuration. The NA transfer becomes important when the dye-semiconductor coupling is weak. Similar to tunneling, the NA transfer rate shows exponential dependence on the donor-acceptor separation.

The dynamics of the electron injection from alizarin to TiO_2 are presented in Fig. 4. The ET is determined by the portion of the electron that has left the dye. The timescales and relative amounts of adiabatic and NA ET are computed by separating the overall ET evolution into the contributions that are due to changes in the localization of the initially occupied state and populations of the initially empty states, respectively. In order to obtain the ET timescale, the total ET is fit by the equation,

$$\mathrm{ET}(t) = \mathrm{ET}_f(1 - \exp\left[-(t + t_0)/\tau\right]), \tag{18}$$

where ET_f is the final amount of ET, and τ is the timescale. The fact that the photoexcited state is initially delocalized onto the surface is reflected by the t_0 term of the fit. The t_0 fitting constant can be interpreted as the time the ET is advanced by the photoexcitation. Due to the delocalization of the photoexcited state onto the semiconductor, Fig. 3, about 25% of the electron is already in the surface after the photoexcitation. The adiabatic and NA ET are fit with a similar equation, but without the t_0 term. The adiabatic mechanism dominates the dynamics and is not only faster but also reaches a much higher amplitude than the NA component. The thin grey lines show 20% of the variance of the data. The variance is quite large, which indicates a large diversity in the individual electron injection events, depending on the initial condition. The small oscillations in the total and adiabatic ET data, relative to the fit line, are similar to those observed by Willig and co-workers with perylene,[82] and are due to coherent nuclear vibrations.

The ET events that originate from the photoexcited states above and below the CB, Fig. 3, show significant differences.[96] The ET dynamics starting in the photoexcited states above the band gap are

qualitatively similar to the average ET dynamics shown in Fig. 4. The photoexcited state is more delocalized and the ET proceeds faster at energies above the CB. Both adiabatic and NA transfer components are faster at the higher energies. Because the DOS increases with energy, Fig. 3, there is a shorter wait until a surface state that is strongly coupled to the dye state is found and adiabatic ET takes place. A larger DOS provides more semiconductor states to interact with, leading to faster NA ET. The electron injection dynamics at high initial energies are even more dominated by the adiabatic mechanism than the dynamics averaged over all initial conditions. In contrast, the ET coordinate and its adiabatic component are markedly different for the initial states that are below the CB edge.[96] The ET is not exponential during the first 8 fs and is best fit by an inverted Gaussian, reflecting the fact that the donor state must enter the CB before crossing with an acceptor state. Once the dye state has moved into the CB, the ET can be fit with an exponential. The state crossing is not required by NA ET, which behaves exponentially even for the lower energy initial conditions. Both adiabatic and NA ET components are slowed down for the initial states below the CB. It is quite remarkable that photoexcitation below the CB can lead to fast and efficient electron injection.[95,96]

4 Excitation Dynamics in Quantum Dots

QDs have the potential to substantially improve the conversion of solar energy into electric current, thereby producing more efficient solar cells. The tunability of the absorption spectrum of QDs with their size circumvents the need for sensitizer chromophores as in the Grätzel cell, Section 3. The control of the charge carrier relaxation pathway with QD type, size and surface passivation creates additional tools for improving photovoltaic devices.

Conversion efficiency is one of the most important parameters to optimize in order to implement photovoltaic cells on a truly large scale.[103] The maximum thermodynamic efficiency for the conversion of unconcentrated solar irradiance into electrical free energy in the radiative limit assuming detailed balance and a single threshold absorber was calculated by Shockley and Queisser[104] in 1961 to be about 31%. QD solar cells have the potential to increase the maximum attainable thermodynamic conversion efficiency of solar photon conversion up to about 66% by utilizing hot photogenerated carriers. There are two fundamental ways to utilize the hot carriers for enhancing the efficiency of photon conversion: by either enhancing the photovoltage or the photocurrent. Enhanced photovoltage requires that the carriers be extracted from the photoconverter before they cool.[105] Enhanced photocurrent requires the energetic hot carriers to produce two or more electron-hole pairs through impact ionization[106] – a process that is the inverse of an Auger process whereby two electron-hole pairs recombine to produce a single highly energetic electron-hole pair. In order to achieve higher voltages, the rates of photogenerated carrier separation, transport, and interfacial transfer across the contacts to the semiconductor must all be fast compared to the rate of carrier cooling.[107] Achieving larger currents requires that the rate of impact ionization be greater than the rates of cooling and other relaxation processes of hot carriers.

Over the past several years many investigations have been published that explore hot electron and hole relaxation dynamics in QDs. The results are controversial. It is quite remarkable that there are so many reports that both support[88,108–120] and contradict[121–127] the prediction of the existence of a phonon bottleneck to the hot-electron cooling in QDs, defined as a strong reduction in the efficiency of electron-phonon interaction. A number of groups have investigated QDs created with III-V semiconductor materials, such as GaAs, InAs and InP, and reported slowed charge-carrier cooling due to the QD quantization effects.[108–113] Relaxation of both hot electrons[108–111,128] and holes[112,113] was considerably slowed down relative to the bulk materials. The studies of QDs of the II-VI type, and CdSe in particular, found two relaxation time scales, whose relative weights depended upon the molecules capping the QDs.[114–119] A phonon bottleneck was observed similar to the III-V QDs. In addition, a new, faster relaxation component was seen and attributed to the Auger mechanism for electron relaxation, whereby the excess electron energy is rapidly transferred to a hole, which then relaxes rapidly through its dense spectrum of states. If the hole is removed and trapped by the molecules capping the QD surface, the Auger mechanism for the hot electron relaxation is inhibited and the overall relaxation time increases. In contradiction, many investigations exist in the literature in which a phonon bottleneck was apparently not observed. These results were reported for both III-V QDs[121–123] and II-VI QDs.[124,125] In some cases[126,127] hot-electron relaxation was found to be slowed only slightly.

The breakthrough in the studies of carrier multiplication came with the observations of multiple electron-hole pairs in PbSe QDs upon absorption of high energy photons.[88,120] The observations immediately

raised the questions of why the alternative relaxation pathways that were effective in QDs made of other materials failed to quench impact ionization in PbSe QDs. Using the FSSH approach implemented within DFT as described in Section 2, we investigate the relaxation mechanisms and establish that both electron and hole relaxation in PbSe QDs is slow, allowing time for the carrier multiplication and eliminating the Auger relaxation pathway that transfer the electron energy to the rapidly relaxing holes.

Electronic States of Quantum Dots

The electronic structure of QDs is intimately related to their quasi-zero-dimensional nature that makes them closer to atoms than bulk materials. For this reason, QDs are often called "artificial atoms", and assemblies of QDs are referred to as "artificial molecules". The reduction in the system dimensionality that accompanies the transition from bulk semiconductors to QDs is associated with a dramatic transformation in the energy spectra, which become discrete and atomic-like. At the qualitative level, the quantum energies of the electron and hole states can be understood by regarding the QD as a spherical potential that confines the non-interacting particles. The lowest states of both electrons and holes have an approximate spherical symmetry and are labeled as S-states. The next three levels show P-like character and are polarized along the x, y, and z-directions.[87,111]

The electronic structure of QDs is exemplified in Figures 5 and 6 with the 32 atom PbSe QD. The simple cubic lattice of bulk PbSe allows one to create the small roughly spherical nanocrystal of about 10Å in diameter that preserves the bulk symmetry. A structural relaxation of the 32 atom PbSe QD relative to the bulk does occur even at zero Kelvin. Temperature induced fluctuations further distort the dot, but cause neither surfaces to reconstruct nor bonds reconnect. The four lowest electronic states shown in Fig. 5 exhibit the expected S- and P-like symmetries, which are significantly modulated by the local atomic structure. The energies of the hole and electron states shown in Fig. 6 fluctuate over time due to thermal nuclear motions. The DOS shown in Fig. 6 is constructed by the broadening of the energy levels with Gaussians of 0.01 eV width. The S-like lowest electron and hole states are clearly isolated from the rest of the states. The arrows in Fig. 6 indicate the energies of the electron and hole excitations. The energy range is set three times larger than the QD energy gap, in correspondence with the experiments.[88] The initial excited states for each nuclear configurations are chosen based on the largest transition dipole moments among the states close to the energies indicated by the arrows.

Phonon-Induced Relaxation of Electrons and Holes

The quantum confinement effects in QDs strongly affect not only the electronic spectrum, but also the rates and pathways of electron-phonon and hole-phonon relaxation. The reduced availability of pairs of electronic states that satisfy energy and momentum conservation leads to a strong reduction in the efficiency of electron-phonon interactions in QDs, i.e. the phonon bottleneck. This effect dramatically slows down energy relaxation in zero-dimensional QDs in comparison to systems of higher dimensionality. Other, non-phonon mechanisms for energy relaxation in QDs include interactions with defects and Auger-type electron-hole interactions involving transfer of the electron excess energy to a hole, with subsequent fast hole relaxation through its dense spectrum of states. The relaxation effects are to be minimized in order to achieve the desired enhancement of the solar photon conversion efficiency.[87]

The DOS of holes calculated for the 10Å PbSe QD shows a denser spectrum, compared to the DOS of electrons, Fig. 6. The separation of the S-like from the main state manifold is more pronounced for the electrons than for the holes. The difference in the electron and hole DOS is not as dramatic in PbSe QDs as, for instance, in the extensively studied CdSe QDs. The simulated relaxation dynamics are slightly faster for the holes than for the electrons, Fig. 7. The difference is minor, which explains why the Auger-type electron relaxation through energy transfer to the hole is not efficient in PbSe. The relaxation times for both holes and electrons exceed 1 ps. This is orders of magnitude longer than the electron injection time in the alizarin-TiO_2 system considered in the previous section, and is several times longer than the closely related electron and hole relaxation times in CNs considered next. It may be expected that the simulation overestimates the relaxation rates, since in experiments the QD surfaces are passivated, decreasing the number of states in the relevant energy range. Comparing the DOS of Fig. 6 with the relaxation dynamics shown in the top panel of Fig. 7, one observes that the initial photoexcitation peak vanishes and re-appears directly at the final P and S-states. Although multiple states are visited by electrons and holes during the relaxation, none of the intermediate states play any special role. The slow and nearly symmetric electron and hole relaxation in the

PbSe QD leads us to conclude that the observed carrier multiplication takes place due to the low rates of the other, unfavorable relaxation mechanisms.

5 Electron and Hole Relaxation in Carbon Nanotubes

Discovered in 1991 by Iijima,[129] CNs continue to be at the forefront of scientific research. Their unique structural, mechanical and electronic properties[130,131] prompt a variety of applications ranging from chemical sensors to computer logic gates and field-effect transistors.[132–138] Advancements in the synthesis and purification of CNs have enabled the study of size-selected tubes as well as rudimentary separation of metallic and semiconducting CNs.[139,140] Developments in the spectroscopic techniques have accompanied the progress in the nanotube preparation. Numerous time-resolved experiments have addressed the electronic structure of CNs, revealing intriguing features in the nanotube response to electronic and optical excitations.[141–149]

Motivated by the time-resolved experimental observations we performed the first real-time *ab initio* simulation of the electron and hole dynamics in a CN. The simulated dynamics agree with the experimental timescales, establish the electron and hole relaxation pathways, characterize the electronic states and phonon modes that facilitate the energy dissipation, and reveal a number of intriguing details of the relaxation processes. In particular, the simulation shows for the nanotube under investigation that the holes relax more slowly than electrons, even though the holes have a denser manifold of states facilitating the relaxation. The electrons show a single exponential decay, while holes relax by a Gaussian and then an exponential component. Both electron and hole relaxation is promoted primarily by the C-C stretching G-type phonons with frequencies around 1500 cm^{-1}. However, holes, but not electrons, additionally couple to the lower frequency breathing modes.

The study described below is performed on the smallest semiconducting (7,0) zig-zag CN, since semiconductors can be simulated with fewer basis functions, and a zig-zag tube has a frequently repeated periodic pattern that helps to reduce the size of the simulation cell. The study is carried out with the SH approach described in the Theory section.

Electronic Structure of Carbon Nanotubes

The nanotube DOS exhibits characteristic van Hove singularities (vHs) due to the folding of the 1D Brillouin zone of a graphene sheet,[130] Figure 8. These singularities dominate the electronic spectrum of CNs. The curvature of the nanotube alters the DOS by creating an asymmetric distribution of states across the Fermi level with the holes having a denser manifold of states than the electrons. The electron and hole relaxation under investigation is initiated by an excitation from the second vHs below the Fermi level to the second vHs above the Fermi level, as in the recent ultrafast laser experiments.[143–145] The states within the singularities were chosen based on the strongest transition dipole moment at a given initial time. The electronic densities of the two most optically active electron and hole states are shown as inserts in Fig. 9. Upon the photoexcitation the electrons and holes relax non-radiatively through the first vHs to their corresponding band edges.

Phonons Facilitating Electron and Hole Relaxation

Figure 9 establishes the types of phonon modes that couple to the electrons and holes and promote the relaxation. The two pairs of states whose densities are shown in the inserts account for 80% of the photoexcitation intensity. FTs of the phonon induced dynamics of the energies of these states are shown in Fig. 9. The FTs identify the modes that modulate the properties of the electron and hole states and create the NA coupling (13). The electron-phonon and hole-phonon coupling occurs over a broad range of frequencies starting at the C-C stretching G-type modes around 1500 cm^{-1} down to the breathing modes below 500 cm^{-1}. The G-modes give the largest contribution to both electron and hole relaxation. In contrast to the electrons, holes also strongly couple to the breathing modes. The coupling of the holes to the lower frequency modes can be understood by considering the energies and densities of the electron and hole states. The lower energy valence band (VB) states supporting the holes have fewer nodes than the higher energy CB states supporting the electrons. The hole states with fewer nodes couple to the lower frequency breathing phonons that also have fewer nodes. The stronger coupling to the breathing modes slows down the hole relaxation dynamics relative to that of the electrons, counteracting the effect of the denser manifold of hole states, Fig. 8, that facilitates the relaxation. Similarly, it can be expected that coupling to lower frequency phonons slows down the hole relaxation in QDs, Section 4, decreasing the rates of phonon heating and Auger relaxation and allowing the carrier multiplication.

Electron and Hole Relaxation Dynamics

Figure 10 details the electron and hole relaxation dynamics in CNs by showing the average electron and hole energies as functions of time. The energy of the electrons is fitted with a single exponential. The energy of the holes gives a poor single exponential fit and is described by a sum of the Gaussian and exponential components. The Gaussian component can be hardly distinguished in the electron relaxation. The exponential component of the hole relaxation is noticeably slower than that of the electrons, which is rather surprising since the holes have a larger DOS, Fig. 8, that facilitates relaxation. The Gaussian component accounts for nearly half of the hole energy relaxation and occurs while the hole spreads within the second vHs and before the Boltzmann weighting produces the exponential decay from the second to the first singularity. The existence of a smaller maximum in the second vHs of the hole DOS may additionally contribute to the Gaussian relaxation component. Minor deviations from the exponential fit seen with the electron energy towards the end of the relaxation are most likely related to the small peak in the electron DOS near the Fermi level, Figs. 8.

The timescales for the electron and hole relaxation from the 2 and 2' singularities to the band edge computed for the (7,0) tube are in good agreement with the reported ultrafast spectroscopy experiments. The experimental results for this type of process vary from tens of femtoseconds[142–144] to picoseconds[145–147] depending on sample preparation, size homogeneity, photoexcitation energy, intensity, and type of experiment. The simulation gravitates towards the slower end of the experimental data and provides an upper bound on the relaxation time, since other relaxation mechanisms, most notably charge-charge scattering and electron-hole annihilation, have not been included in the simulation.

6 Conclusions

The three case-studies described above provide a sampling of the exciting phenomena observed with nanomaterials in the very recent past. The state-of-the-art theoretical tools developed in our group allowed us to characterize the excitation dynamics in these nanomaterials, establish the mechanisms of charge transfer and relaxation, and uncover a number of interesting and practically important features that are accessible only from simulation and that explain the unexpected experimental observations.

We showed that the ultrafast electron injection takes place in the alizarin-TiO_2 system not through the commonly assumed coupling to multiple bulk states of the semiconductor, but through a strong coupling to a few surface states. The established injection mechanism does not require a high density of acceptor states and, therefore, can function at the energies close to the edge of the conduction band. Electron injection at those energies avoids energy losses, helping to preserve the maximum voltage attainable in the Grätzel solar cell.

We found that the phonon-induced electron and hole relaxation in the PbSe quantum dots is almost symmetric and occurs slowly, on a longer than one picosecond timescale. The slow phonon-assisted relaxation allows for the other productive processes to occur. The carrier multiplication that generates multiple electron-hole pairs and increases the current attainable in a solar cell becomes possible, since both the direct electron and hole cooling and the Auger assisted electron relaxation through hole states are inefficient.

We determined the pathways of relaxation of free charge carriers in carbon nanotubes. The simulations agreed with the available experimental data and provided important insights into the decay mechanisms of the excited electrons and holes. The non-trivial observations included the dominant role of the high frequency phonons in both electron and hole relaxation, and the substantial contribution of the low frequency breathing modes to the dynamics of holes, but not electrons. These facts rationalized why holes decayed slower and over multiple timescales, despite their denser manifold of states that was expected to facilitate faster relaxation.

The simulations performed with the specific systems and addressing concrete experimental observations and practical questions bear on a much wider spectrum of problems. The interfacial charge transfer is generic to molecular electronics, where the contacts between molecular conductors and bulk electron leads remain very poorly understood. The slow charge relaxation in the QD establishes the existence of a phonon bottleneck that can be used to achieve not only carrier multiplication and larger solar cell currents, but also better voltages through delayed carrier cooling. The hole-phonon and electron-phonon interaction timescales seen in our studies establish limits on vibrationally induced dephasing that is critical to avoid for spintronic and quantum computing applications of quantum dots. The heating mechanisms seen in the simulations

of carbon nanotubes are critical for successful development of nanotube-based miniature electronic devices. The systems and problems considered here contribute to a general framework for control and utilization of the novel phenomena that become possible on the nanoscale.

Acknowledgments

The financial support of NSF CAREER Award CHE-0094012, PRF Award 150393, and DOE Award DE-FG02-05ER15755 is gratefully acknowledged.

References

1. M. A. L. Marques and E. K. U. Gross, Annu. Rev. Phys. Chem. **55**, 427 (2004).
2. T. Frauenheim, G. Seifert, M. Elstner, T. Niehaus, C. Köhler, M. Amkreutz, M. Sternberg, Z. Hajnal, A. DiCarlo, and S. Suhai, J. Phys. Cond. Matter **14**, 3015 (2002).
3. A. Szabo and N. S. Ostlund, *Modern Quantum Chemsitry*, 1st revised ed. (McGraw-Hill, Inc., New York, 1989).
4. G. Kresse and J. Furthmüller, Comput. Mater. Sci. **6**, 15 (1996).
5. G. Kresse and J. Furthmüller, Phys. Rev. B **54**, 11169 (1996).
6. W. Kohn and L. J. Sham, Phys. Rev. A **4**, 1133 (1965).
7. R. Baer, T. Seideman, S. Ilani, and D. Neuhauser, J. Chem. Phys. **120**, 3387 (2004).
8. I. Franco and S. Tretiak, J. Am. Chem. Soc. **126**, 12130 (2004).
9. M. A. L. Marques, X. López, D. Varsano, A. Castro, and A. Rubio, Phys. Rev. Lett. **90**, 258101 (2003).
10. J. P. Perdew, K. Burke, and M. Ernzerhof, Phys. Rev. Lett. **77**, 3685 (1996).
11. S. Hammes-Schiffer and J. C. Tully, J. Chem. Phys. **101**, 4657 (1994).
12. A. D. McLachlan, R. D. Gregory, and M. A. Ball, Mol. Phys. **7**, 119 (1963-64).
13. G. D. Billing, Int. Rev. Phys. Chem. **13**, 309 (1994).
14. J. C. Tully, in *Classical and Quantum Dynamics in Condensed Phase Simulations*, edited by B. J. Berne, G. Ciccotti, and D. F. Coker (World Scientific, Singapore, 1998), pp. 489–514.
15. J. C. Tully and R. K. Preston, J. Chem. Phys. **55**, 562 (1971).
16. J. C. Tully, J. Chem. Phys. **93**, 1061 (1990).
17. P. V. Parahdekar and J. C. Tully, J. Chem. Phys. **122**, 094102 (2005).
18. M. F. Herman, J. Chem. Phys. **103**, 8081 (1995).
19. D. F. Coker and L. Xiao, J. Chem. Phys. **102**, 496 (1995).
20. Y. L. Volobuev, M. D. Hack, M. S. Topaler, and D. G. Truhlar, J. Chem. Phys. **112**, 9716 (2000).
21. M. D. Hack and D. G. Truhlar, J. Chem. Phys. **114**, 9305 (2001).
22. A. W. Jasper, S. N. Stechmann, and D. G. Truhlar, J. Chem. Phys. **116**, 5424 (2002).
23. S. Nielsen, R. Kapral, and G. Ciccotti, J. Chem. Phys. **6543**, 112 (2000).
24. M. Kernan, G. Ciccotti, and R. Kapral, J. Chem. Phys. **116**, 2346 (2002).
25. O. V. Prezhdo and V. V. Kisil, Phys. Rev. A **56**, 162 (1997).
26. R. W. Wyatt, C. L. Lopreore, and G. Parlant, J. Chem. Phys. **114**, 5113 (2001).
27. F. A. Webster, P. J. Rossky, and R. A. Friesner, Comp. Phys. Comm. **63**, 494 (1991).
28. E. R. Bittner and P. J. Rossky, J. Chem. Phys. **103**, 8130 (1995).
29. O. V. Prezhdo and P. J. Rossky, J. Chem. Phys. **107**, 825 (1997).
30. O. V. Prezhdo, J. Chem. Phys. **111**, 8366 (1999).
31. C. F. Craig, W. R. Duncan, and O. V. Prezhdo, Phys. Rev. Lett. (2005), in press.
32. A. Donoso and C. C. Martens, Phys. Rev. Lett. **87**, 223202 (2001).
33. C. L. Lopreore and R. E. Wyatt, Phys. Rev. Lett. **82**, 5190 (1999).
34. E. R. Bittner and R. E. Wyatt, J. Chem. Phys. **113**, 8888 (2000).
35. E. Gindensperger, C. Meier, and J. A. Beswick, J. Chem. Phys. **113**, 9369 (2000).
36. O. V. Prezhdo and C. Brooksby, Phys. Rev. Lett. **86**, 3215 (2001).
37. A. S. Sanz and S. Miret-Artes, J. Chem. Phys. **122**, 014702 (2005).
38. K. Runge and D. A. Micha, Phys. Rev. A **62**, 022703 (2000).
39. D. A. Micha and B. Thorndyke, Adv. Quant. Chem. **47**, 293 (2004).
40. E. Deumens and Y. Ohrn, J. Phys. Chem. A **105**, 2660 (2001).
41. R. Cabrera-Trujillo, J. R. Sabin, E. Deumens, and Y. Ohrn, Adv. Quant. Chem. **47**, 253 (2004).
42. W. H. Thompson, J. Chem. Phys. **118**, 1059 (2003).
43. I. Burghardt, K. B. Moller, G. Parlant, L. S. Cederbaum, and E. R. Bittner, Int. J. Quant. Chem. **100**, 1153 (2004).
44. I. Burghardt, J. Chem. Phys. **122**, 094103 (2005).

45. S. Bonella and D. F. Coker, J. Chem. Phys. **122**, 194102 (2005).
46. P. Ehrenfest, Z. Physik **45**, 455 (1927).
47. T. N. Todorov, J. Hoekstra, and A. P. Sutton, Phys. Rev. Lett. **86**, 3606 (2001).
48. A. P. Horsfield, D. R. Bowler, A. J. Fisher, T. N. Todorov, and C. G. Sanchez, J. Phys. - Cond. Mat. **16**, 8251 (2004).
49. O. V. Prezhdo and Y. V. Pereverzev, J. Chem. Phys. **113**, 6557 (2000).
50. C. Brooksby and O. V. Prezhdo, Chem. Phys. Lett. **346**, 463 (2001).
51. O. V. Prezhdo and Y. V. Pereverzev, J. Chem. Phys. **116**, 4450 (2002).
52. E. Pahl and O. V. Prezhdo, J. Chem. Phys. **116**, 8704 (2002).
53. O. V. Prezhdo, J. Chem. Phys. **117**, 2995 (2002).
54. C. Brooksby and O. V. Prezhdo, Chem. Phys. Lett. **378**, 533 (2003).
55. D. Kilin, Y. V. Pereverzev, and O. V. Prezhdo, J. Chem. Phys. **120**, 11209 (2004).
56. E. Heatwole and O. V. Prezhdo, J. Chem. Phys. **121**, 10967 (2004).
57. E. Heatwole and O. V. Prezhdo, J. Chem. Phys. **122**, 234109 (2005).
58. O. V. Prezhdo and P. J. Rossky, Phys. Rev. Lett. **81**, 5294 (1998).
59. O. V. Prezhdo, Phys. Rev. Lett. **85**, 4413 (2000).
60. A. Luis, Phys. Rev. A **67**, 062113 (2003).
61. P. Exner, J. Phys. A - Math. Gen. **38**, L449 (2005).
62. A. Nitzan and M. A. Ratner, Science **300**, 1384 (2003).
63. P. A. Derosa and J. M. Seminario, J. Phys. Chem. B **105**, 471 (2001).
64. X. Y. Zhu, J. Phys. Chem. B **108**, 8778 (2004).
65. M. W. Holman, R. Liu, and D. M. Adams, J. Am. Chem. Soc. **125**, 12649 (2003).
66. F. F. Fan, Y. Yao, L. Cai, L. Cheng, J. M. Tour, and A. J. Bard, J. Am. Chem. Soc. **126**, 4035 (2004).
67. D. L. Jiang, H. J. Zhao, S. Q. Zhang, and R. John, J. Catal. **223**, 212 (2004).
68. W. Zhao, W. H. Ma, C. C. Chen, J. C. Zhao, and Z. G. Shuai, J. Am. Chem. Soc. **126**, 4782 (2004).
69. T. Hirakawa, J. K. Whitesell, and M. A. Fox, J. Phys. Chem. B **108**, 10213 (2004).
70. P. D. Cozzoli, E. Fanizza, R. Comparelli, M. L. Curri, A. Agostiana, and D. Laub, J. Phys. Chem. B **108**, 9623 (2004).
71. H. G. Kim, D. W. Hwang, and J. S. Lee, J. Am. Chem. Soc. **126**, 8912 (2004).
72. D. Liu, G. L. Hug, and P. V. Kamat, J. Phys. Chem. **99**, 16768 (1995).
73. B. Oregan and M. Grätzel, Nature **353**, 737 (1991).
74. O. Schwarz, D. van Loyen, S. Jockusch, N. J. Turro, and H. Duerr, J. Photochem. Photobiol. A: Chem. **132**, 91 (2000).
75. R. D. McConnell, Renew. Sustain. Energy Rev. **6**, 273 (2002).
76. J. B. Asbury, E. C. Hao, Y. Q. Wang, H. N. Ghosh, and T. Q. Lian, J. Phys. Chem. B **105**, 4545 (2001).
77. T. Hannappel, B. Burfeindt, W. Storck, and F. Willig, J. Phys. Chem. B **101**, 6799 (1997).
78. N. A. Anderson, E. Hao, X. Ai, G. Hastings, and T. Lian, Physica E. **14**, 215 (2002).
79. R. Huber, S. Spoerlein, J. E. Moser, M. Grätzel, and J. Wachtveitl, J. Phys. Chem. B **104**, 8995 (2000).
80. R. Huber, J. E. Moser, M. Grätzel, and J. Wachtveitl, J. Phys. Chem. B **106**, 6494 (2002).
81. S. Ramakrishna and F. Willig, J. Phys. Chem. B **104**, 68 (2000).
82. S. Ramakrishna, F. Willig, V. May, and A. Knorr, J. Phys. Chem. B **107**, 607 (2003).
83. E. Kucur, J. Reigler, G. A. Urban, and T. Nann, J. Chem. Phys. **120**, 1500 (2004).
84. W. Greens, T. Martens, J. Poortmans, T. A. J. Manca, L. Lutsen, P. Heremans, S. Borghs, R. Mertens, and D. Vanderzande, Thin Solid Films **451-452**, 498 (2004).
85. E. Hao, N. A. Anderson, J. B. Asbury, and T. Lian, J. Phys. Chem. B **106**, 10191 (2002).
86. P. Ravirajan, S. A. Haque, D. Poplavskyy, J. R. Durrant, D. D. C. Bradley, and J. Nelson, Thin Solid Films **451-452**, 624 (2004).
87. A. J. Nozik, Physica E **14**, 115 (2001).
88. R. D. Schaller and V. I. Klimov, Phys. Rev. Lett. **92**, 186601 (2004).
89. L. X. Wang and V. May, J. Chem. Phys. **121**, 8039 (2004).
90. M. Thoss, I. Kondov, and H. Wang, Chem. Phys. **304**, 169 (2004).
91. L. G. C. Rego and V. S. Batista, J. Am. Chem. Soc. **125**, 7989 (2003).
92. W. Stier and O. V. Prezhdo, J. Mol. Struct. (Theochem) **630**, 33 (2002).
93. W. Stier and O. V. Prezhdo, J. Phys. Chem. B **106**, 8047 (2002).
94. W. Stier and O. V. Prezhdo, Isr. J. Chem. **42**, 213 (2002).
95. W. Stier, W. R. Duncan, and O. V. Prezhdo, Adv. Mat. **16**, 240 (2004).
96. W. R. Duncan, W. M. Stier, and O. V. Prezhdo, J. Am. Chem. Soc. **127**, 7941 (2005).
97. W. R. Duncan and O. V. Prezhdo, J. Phys. Chem. B **109**, 365 (2005).
98. W. R. Duncan and O. V. Prezhdo, J. Phys. Chem. B (2005), in press.
99. J. Kruger, U. Bach, and M. Grätzel, Adv. Mater. **12**, 447 (2000).

100. A. C. Arango, L. R. Johnson, V. N. Bliznyuk, Z. Schlesinger, S. A. Carter, and H. H. Horhold, Adv. Mater. **12**, 1689 (2001).
101. A. F. Nogueira, J. R. Durrant, and M. A. D. Paoli, Adv. Mater. **13**, 826 (2001).
102. M. Grätzel, J Photochem. Photobiol. C: Photochem. Rev **4**, 145 (2003).
103. M. A. Green, *Third generation photovoltaics* (Bridge Printery, Sydney, 2001).
104. W. Shockley and H. J. Queisser, J. Appl. Phys. **32**, 510 (1961).
105. D. S. Boudreaux, F. Williams, and A. J. Nozik, J. Appl. Phys. **51**, 2158 (1980).
106. S. Kolodinski, J. H. Werner, T. Wittchen, and H. J. Queisser, Appl. Phys. Lett. **63**, 2405 (1993).
107. F. Williams and A. J. Nozik, Nature **311**, 21 (1984).
108. H. Yu, S. Lycett, C. Roberts, and R. Murray, Appl. Phys. Lett **69**, 4087 (1996).
109. M. Sugawara, K. Mukai, and H. Shoji, Appl. Phys. Lett **71**, 2791 (1997).
110. B. N. Murdin, A. R. Hollingworth, M. Kamal-Saadi, R. T. Kotitschke, and C. N. Cielsla, Phys. Rev. B **59**, R7817 (1999).
111. R. J. Ellingson, J. L. Blackburn, P. Yu, G. Rumbles, O. I. Micic, and A. J. Nozik, J. Phys. Chem. B **106**, 7758 (2002).
112. R. Heitz, M. Veit, N. N.Lebentsov, A. Hoffmann, and D. Bimberg, Phys. Rev. B **56**, 10435 (1997).
113. F. Adler, M. Geiger, A. Bauknecht, D. Haase, and P. Ernst, J. Appl. Phys. **83**, 1631 (1998).
114. P. Guyot-Sionnest, M. Shim, C. Matranga, and M. Hines, Phys. Rev. B **60**, R2181 (1999).
115. V. I. Klimov, A. A. Mikhailovsky, D. W. McBranch, C. A. Leatherdale, and M. G. Bawendi, Phys. Rev. B **61**, R13349 (2000).
116. M. Achermann, J. A. Hollingsworth, and V. I. Klimov, Phys. Rev. B **68**, 245302 (2003).
117. R. G. Ispasiou, J. Lee, F. Papadimitrakopoulos, and T. Goodson, Chem. Phys. Lett. **340**, 7 (2001).
118. M. B. Mohamed, C. Burda, and M. A. El-Sayed, Nano Lett. **1**, 589 (2001).
119. P. Yu, J. M. Nedeljkovic, P. A. Ahrenkiel, R. J. Ellingson, and A. J. Nozik, Nano Lett. **4**, 1089 (2004).
120. R. J. Ellingson, M. C. Beard, J. C. Johnson, P. R. Yu, O. I. Micic, A. J. Nozik, A. Shabaev, and A. L. Efros, Nano Lett. **5**, 865 (2005).
121. M. Lowisch, M. Rabe, F. Kreller, and F. Henneberger, Appl. Phys. Lett **74**, 2489 (1999).
122. X.-Q. Li, H. Nakayama, and Y. Arakawa, Jpn. J. Appl. Phys. **38**, 473 (1999).
123. I. Gontijo, G. S. Buller, J. S. Massa, A. C. Walker, and S. V. Zaitsev, Jpn. J. Appl. Phys. **38**, 674 (1999).
124. U. Woggon, H. Giessen, F. Gindele, O. Wind, B. Fluegel, and N. Peyghambarian, Phys. Rev. B **54**, 17681 (1996).
125. V. I. Klimov and D. W. McBranch, Phys. Rev. Lett. **80**, 4028 (1998).
126. T. S. Sosnowski, T. B. Norris, H. Jiang, J. Singh, K. Kamath, and P. Bhattacharya, Phys. Rev. B **57**, R9423 (1998).
127. R. Heitz, M. Veit, A. Kalburge, Q. Zie, and M. Grundmann, Physica E **2**, 578 (1998).
128. K. Mukai and M. Sugawara, Jpn. J. Appl. Phys. **37**, 5451 (1998).
129. S. Iijima, Nature **354**, 56 (1991).
130. R. Saito, G. Dresselhaus, and M. S. Dresselhaus, *Physical Properties of Carbon Nanotubes* (Imperial College Press, London, 1998).
131. R. H. Baughman, A. A. Zakhidov, and W. A. de Heer, Science **297**, 787 (2002).
132. Y. Wang *et al.*, Science **85**, 2607 (2004).
133. J. Kong *et al.*, Science **287**, 622 (2000).
134. N. Mason, M. J. Biercuk, and C. M. Marcus, Science **303**, 655 (2004).
135. M. S. Strano *et al.*, Science **301**, 1519 (2003).
136. S. G. Rao, L. Huang, W. Setyawan, and S. Hong, Nature **425**, 36 (2003).
137. S. J. Tans *et al.*, Nature **386**, 474 (1997).
138. M. S. Dresselhaus, Nature **432**, 959 (2004).
139. R. Krupke, F. Hennrich, H. v. Lohneysen, and M. M. Kappes, Science **301**, 2003 (2003).
140. M. J. O'Connell *et al.*, Science **297**, 787 (2002).
141. Y. C. Chen *et al.*, Applied Physics Letters **81**, 975 (2002).
142. T. Hertel and G. Moos, Chem. Phys. Rev. **320**, 359 (2000).
143. Y.-Z. Ma *et al.*, J. Chem. Phys. **120**, 3368 (2004).
144. C. Manzoni, A. Gambetta, E. Menna, M. Meneghetti, G. Lanzani, and G. Cerullo, Phys. Rev. Lett. **94**, 207401 (2005).
145. G. N. Ostojic, S. Zaric, J. Kono, M. S. Strano, V. C. Moore, R. H. Hauge, and R. E. Smalley, Phys. Rev. Lett. **92**, 117402 (2004).
146. L. Huang, H. N. Pedrosa, and T. D. Krauss, Phys. Rev. Lett. **93**, 017403 (2004).
147. F. Wang, G. Dukovic, L. E. Brus, and T. F. Heinz, Phys. Rev. Lett. **92**, 177401 (2004).
148. H. Htoon, M. J. O'Connell, S. K. Doorn, and V. I. Klimov, Phys. Rev. Lett. **94**, 127403 (2005).
149. S. Roche, J. Jiang, F. Triozon, and R. Saito, Phys. Rev. Lett. **95**, 076803 (2005).

Figure Captions

Figure 1: Dye-sensitized TiO_2. Upon photoexcitation, alizarin chemisorbed onto the TiO_2 surface transfers an electron into the semiconductor. The ground state of alizarin is in the gap between the valence band (VB) and conduction band (CB). The excited state of alizarin is energetically near the edge of the semiconductor CB, and non-trivial electron injection dynamics ensues as the state crosses in and out of the band.

Figure 2: Evolution of the photoexcited (thick line) and CB (thin lines) state energies in alizarin-sensitized TiO_2. The energy of the photoexcited state energy by about 0.15 eV due to atomic motions. The fluctuation is small relative to the 2.5 eV excitation energy, but it moves the dye state into and out of the TiO_2 CB. **Insert**: Fourier transform of the photoexcited state energy shows low frequency peaks associated with alizarin and surface atoms motions up to the 1600 cm^{-1} frequency of the C-C stretching.

Figure 3: Localization of the photoexcited state on alizarin (circles) and the TiO_2 DOS (solid line) as functions of energy. Below the CB (filled circles) the photoexcited state is localized on the dye. Above the CB (empty circles) the state is significantly delocalized into the semiconductor. The delocalization parallels the increasing TiO_2 DOS. The large spread of the localizations inside the CB is due to fluctuations in the chromophore-semiconductor interaction.

Figure 4: ET dynamics in the alizarin-TiO_2 system averaged over 900 initial conditions and separated into the adiabatic and NA components. The thin grey lines represent 20% of the variance in the ET data. The thick black lines are fits by Eq. (18) with the timescales shown on the figure.

Figure 5: Geometric structure of the PbSe QD under investigation and the spatial densities of its 4 lowest electron states. The simple cubic lattice of PbSe creates a stable 32 atom QD that preserves the bulk structure. The quantum energy levels of electrons and holes can be qualitatively understood by considering a particle in a spherical well. The lowest energy level of both electron and hole is S-like, the next three levels are P-like, etc.

Figure 6: DOS of the PbSe QD. The DOS fluctuates over time due to thermally induced nuclear motions. The arrows indicate the energies of the initial electron and hole excitations, which are set up to match the triple energy gap as in the experiments.[88]

Figure 7: Evolution of the electron and hole excitations in the QD averaged over 500 initial conditions. The top panel shows DOS multiplied by the time-dependent populations of the excited states. The bottom panel gives the average electron and hole energies.

Figure 8: DOS of the (7,0) zig-zag CN. The electron is optically excited between the second van-Hove singularities 2'→2. The electron and hole then decay to the first singularities 1' and 1 on a subpicosecond timescale.

Figure 9: Fourier transforms of the energies of the two most optically active states of electrons and holes in the CN. The insert shows the charge densities of these states. The C-C stretching G-modes around 1500 cm^{-1} strongly couple to both electron and holes. The breathing modes at and below 500 cm^{-1} have fewer nodes and, as a result, better couple to the holes, whose states are lower in energy and also have fewer nodes than the electron states.

Figure 10: Relaxation of the average energy of electrons and holes in the CN. The holes show Gaussian and exponential regimes, while the electrons follow a single exponential. The hole exponential decay is slower than that of the electrons, in spite of the higher density of hole states, Fig. 8, that facilitates faster relaxation. The slow dynamics of the holes can be attributed to the coupling with the low frequency breathing modes, Fig. 9.

Figure 1

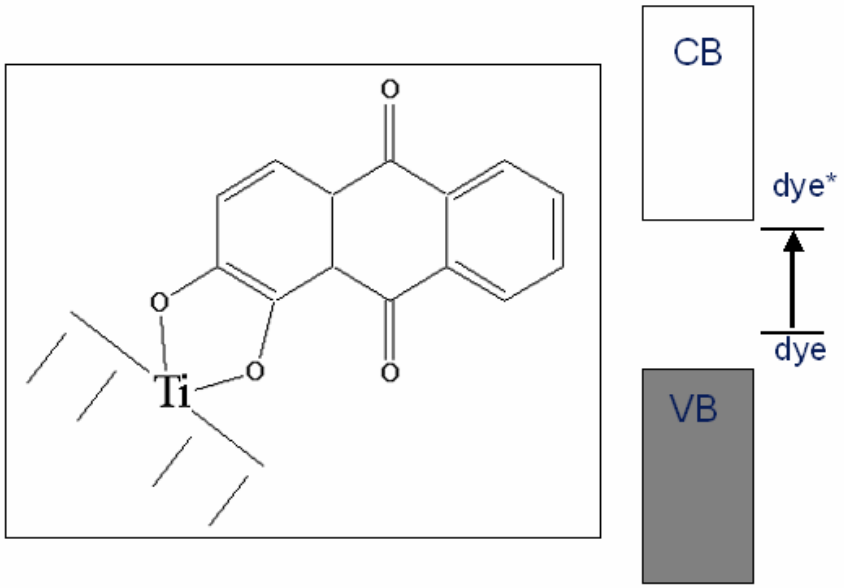

Figure 2

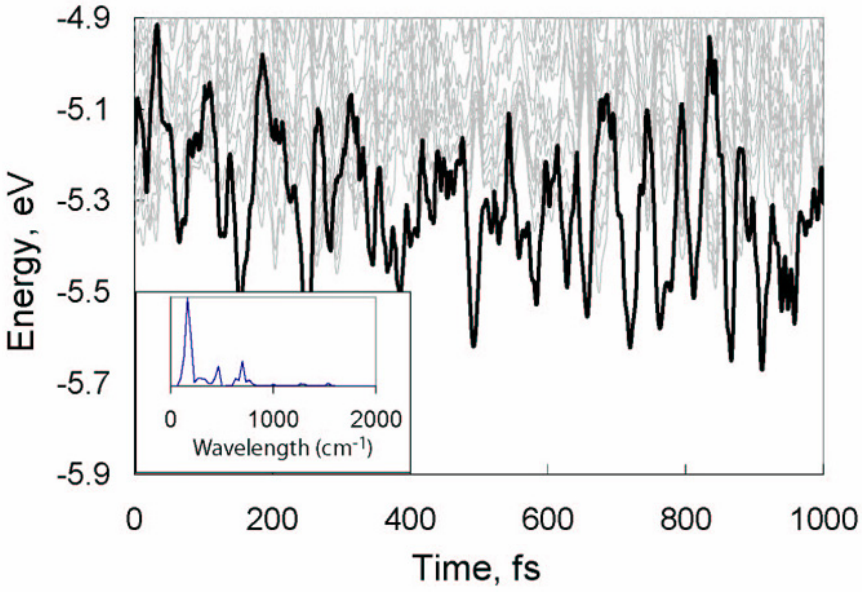

Figure 3

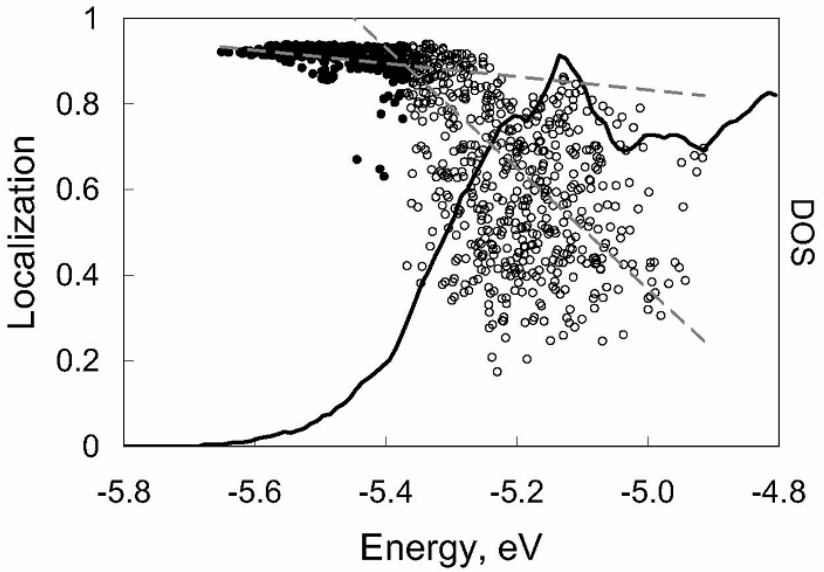

Figure 4

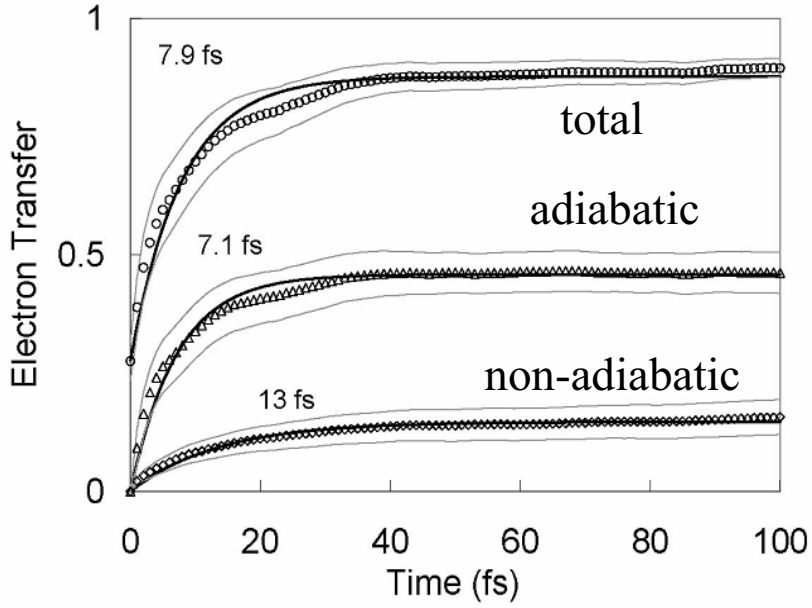

Figure 5

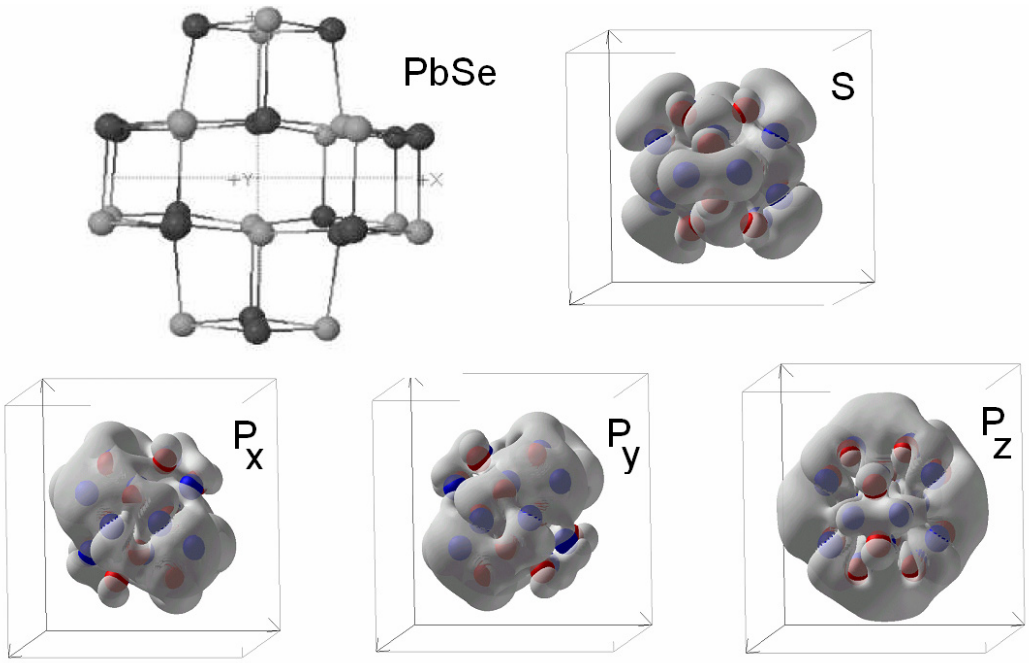

Figure 6

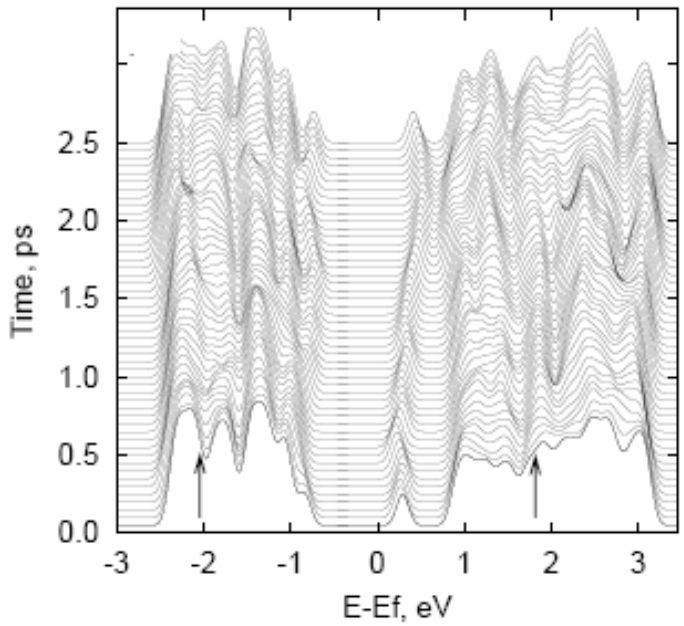

Figure 7

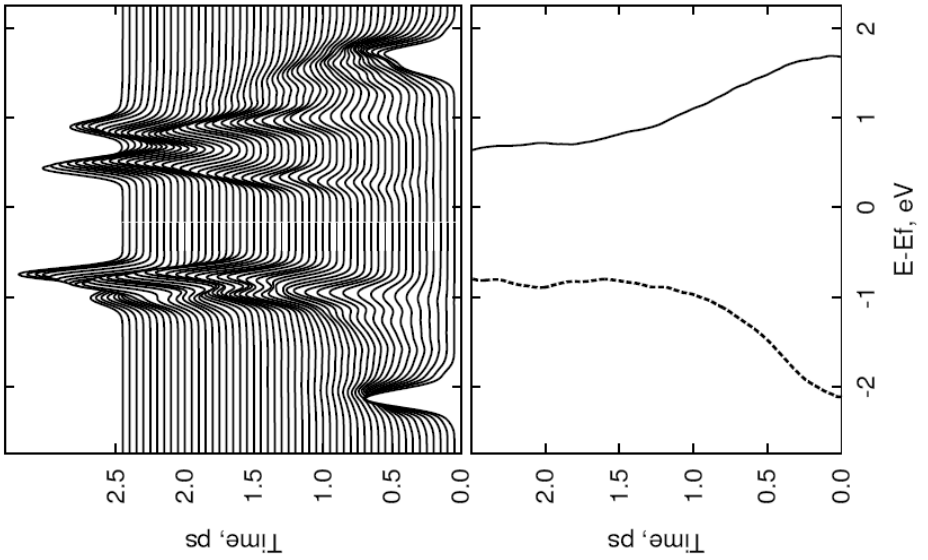

Figure 8

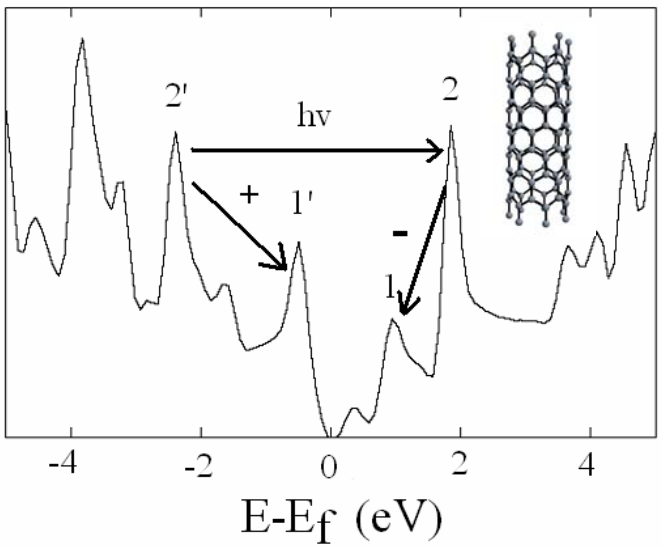

Figure 9

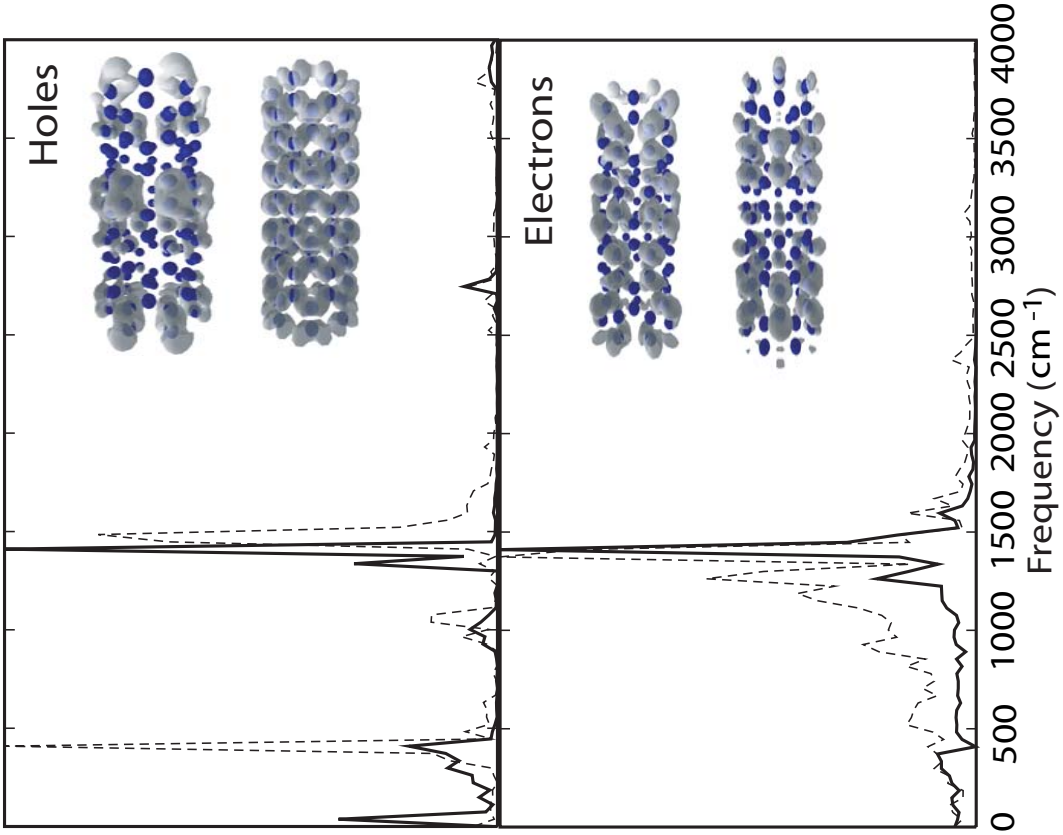

Figure 10